Ocean Modelling 70 (2013) 166–173

Contents lists available at SciVerse ScienceDirect

Ocean Modelling

journal homepage: www.elsevier.com/locate/ocemod

Wave buoy measurements at the Antarctic sea ice edge compared with an enhanced ECMWF WAM: Progress towards global waves-in-ice modelling

Martin J. Doble [a,*], Jean-Raymond Bidlot [b]

[a] UPMC Univ Paris 06, UMR 7093, LOV, Observatoire Océanologique, F-06234 Villefranche-sur-mer, France
[b] European Centre for Medium Range Weather Forecasts, Reading, United Kingdom

ARTICLE INFO

Article history:
Available online 14 June 2013

Keywords:
Sea ice
Waves

ABSTRACT

The breakup of pack ice in the Weddell Sea is examined with respect to a single wave buoy, frozen into the pack ice six months earlier, and the ECMWF WAM model. The pack ice broke up around the buoy on 14th September 2000 as large amplitude storm waves approached the ice edge at the buoy's location. The WAM model is modified to allow waves to propagate into the ice cover, in contrast to the operational scheme which sets wave energy to zero at ice concentrations over 30%. A simple, lookup-table-based, wave scattering attenuation scheme is then added and is combined with a sea ice drag attenuation parameterisation. WAM results at the location of the buoy are compared to the observations over a two-month period straddling the breakup. The modified WAM scheme generally reproduces the significant wave height, wave period and spectral characteristics measured by the buoy, though the model does not yet have any concept of floe breaking and re-freezing, assuming only that the ice cover is broken if the concentration is less than 80%. The simplistic nature of these modifications is designed to allow operational implementation, to eventually provide a global assessment of the wave-influenced ice zone.

1. Introduction

The role of waves in controlling the breakup, position and melt of sea ice is becoming more widely acknowledged, particularly with the emergence of large areas of open water in the summer Central Arctic basin. These long fetches allow the generation of significant wave fields within the Arctic itself and increased significant wave height (SWH) has been observed as a result (Francis et al., 2011). Near the ice edge, waves penetrate into the pack, breaking ice up into floes a few tens of metres across and forming a region known as the marginal ice zone (MIZ). Recent work has suggested that the mechanical break-up of sea ice by waves, tides and large-scale dynamic events was heavily implicated in the dramatic loss of Arctic sea ice in the summer of 2007 (Perovich et al., 2008). Swell waves were observed to break heavily rotted multi-year ice in the Canadian Arctic during summer 2009 (Barber et al., 2009; Asplin et al., 2012). These mechanical processes act to enhance melt rates due to increased open water for absorption of solar radiation and a greater lateral perimeter as floe size diminishes (Steele, 1992; Steer et al., 2008; Toyota et al. (2011)).

Though the changing Arctic is the driving factor in the recent resurgence of waves studies, the Antarctic ice edge has always been exposed to the sustained wave action from the encircling Southern Ocean. The Weddell Sea in particular provides a natural laboratory to follow breakup events as deep low-pressure systems – bred in the Amundsen–Bellingshausen Sea – move eastwards across the region, bringing high winds and associated daunting waves.

Very little wave data exist to examine such breakup, however. This is primarily due to previous technological limitations: until recently it has not been feasible to deploy instruments for long periods since the internally-recording devices required constant attention and were relatively power-hungry (*e.g.* Squire and Moore, 1980; Wadhams et al. 1988; Liu et al., 1991). Such measurements were necessarily conducted on a short term basis, before recovery of the buoys. Only recently has technology advanced to provide adequate bandwidth over satellite links and relatively low-power microprocessors to allow long-term deployment options. A successful long-term drifting wavebuoy array was finally deployed into the advancing Weddell Sea ice edge in April 2000, by the author (MJD), and those data are examined here.

In contrast, much theoretical development has taken place in the past 40 years, with diverse approaches to modelling wave propagation and attenuation (summarised in Squire et al. 1995; Squire, 2007; Broström and Christensen, 2008). The focus is now moving to practical implementations of such schemes, simplifying the sophisticated (and computationally intensive) mathematical

* Corresponding author. Tel.: +33 493763732.
E-mail address: doble@obs-vlfr.fr (M.J. Doble).

1463-5003/$ - see front matter © 2013 Elsevier Ltd. All rights reserved.
http://dx.doi.org/10.1016/j.ocemod.2013.05.012

models to allow their application to real-world situations (*e.g.* Kohout and Meylan, 2008; Vaughan and Squire, 2011; Bennetts and Squire 2012a; Williams et al. 2012). The ultimate goal is to include wave parameterisations in global coupled models, and the first steps are now being taken towards this end (*e.g.* Dumont et al., 2011).

The focus of the current paper is to implement simple wave attenuation schemes, based on recent theoretical developments, on a global scale. To this end, the ECMWF wave model is modified to allow the propagation of waves into the sea ice covered areas – previously WAM set wave energy to zero at the 30% ice concentration boundary. The ultimate goal is to allow WAM to be used operationally to delineate the wave-influenced zone in any ice cover. We limit our approach to areas near and around the MIZ where (a) the wave energy is significant and thus meaningful to model; and (b) where wave scattering by ice floes is the dominant mechanism of wave attenuation (*i.e.* where the MIZ is relatively diffuse). Other scattering mechanisms by cracks and pressure ridges are also present but are more likely to be significant in more continuous ice fields (Bennetts and Squire, 2012b). It has recently been shown that small icebergs can collectively have an impact on the waves (Ardhuin et al. 2011) but such small icebergs are currently not represented in the sea ice data available to ECMWF and this effect is ignored here.

To this end, we incorporate one attenuation scheme based on a wave scattering model, combine it with a sea ice drag attenuation parameterisation within WAM and compare results with wavebuoy measurements as that buoy approaches the ice edge. We first describe the field experiment and wavebuoy, then introduce the basic WAM model, with our enhancements that allow waves to propagate into the ice cover. Results from WAM and buoy are compared in terms of significant wave height, mean and peak period over a two-month timespan, as well as examining selected power spectral density plots from both sources. Impact over the open ocean, where altimeter wave height observations are available, is also assessed.

2. Data and model description

2.1. Buoy observations

We present results from a single drifting buoy as it approached the Weddell Sea ice edge from the interior pack ice, during the period August to October (the Austral spring) 2000. The buoy was the last surviving member of a six-buoy array, deployed into advancing pancake ice at the ice edge on April 18th of the same year. Those deployments are described in detail in previous papers (Doble et al., 2003; Doble and Wadhams, 2006; Doble, 2009). Fig. 1 shows the total buoy track, from deployment until it finally ceased transmission on 13th October 2000. The track is superimposed on the satellite passive microwave SSM/I-derived ice concentrations for the day (13th September) that the pack ice broke up at the buoy location, under the influence of exceptional waves as a storm centre crossed the ice edge. Also shown is (in the open water) is the SWH of that storm at the time of breakup: more than 14 m as the storm centre crossed the ice edge close to the buoy.

The effect of the storm on the surrounding ice can be seen in Fig. 2, which presents the latitude of the 10% and 60% ice concentration contours at the buoy's longitude, as derived from SSM/I satellite data. In the first half of the period considered, the ice edge is advancing northwards at a relatively constant rate of around 15 km per day. The buoy travels north slightly more rapidly, at around 16 km per day, and is initially around 200 km south of the ice edge and more than 300 km from open water. On 12th September the ice begins to feel the influence of an approaching low pressure system, with its leading strong northerly winds. The storm drives the 60% concentration contour southwards by more than 190 km, south of 59° latitude, past the location of the buoy. The vertical dashed line indicates the time at which the buoy wave spectra indicate that the ice broke up. The buoy is driven southwards (by around half a degree, or 55 km) before resuming its northward progress, now in the MIZ north of the 60% contour, where it remained until the final week of transmissions. The ice edge is once again driven south at the end of the dataset, indicating the approach of a second storm (which the buoy did not survive).

The buoy was instrumented with a Crossbow CXL02LF2Z vertical accelerometer (±2G), which was sampled every three hours, at 2 Hz over a period of 25.6 min for a total of 3072 samples. The accelerometer data was processed by the Persistor CF1 microprocessor on board the buoy and the resulting one-dimensional spectra transmitted over an *Orbcomm* satellite link. The on-board scheme first double integrates the acceleration data to derive displacement, applying a 513-point moving average high-pass filter to remove any low frequency drift. The signal was passed through an anti-alias filter of 0.7 Hz shoulder frequency prior to digitisation. To achieve the smallest possible variance per data point, data were then split into 1024 sample segments, windowed with a triangular Parzen function and overlapped by half their length. A Fast Fourier Transform (FFT) was then performed on each segment, averaging the results together in time (4 segments) and in frequency (three bins combined below 0.1 Hz, five bins combined above 0.1 Hz). The resulting wave spectrum is defined at 55 frequencies from 0.025 to 0.5 Hz, with 27 degrees of freedom (DoF) at low frequency and 46 at high frequency.

High mean and peak periods (>18 and >25 s respectively) were reported by the buoy during calm periods or when enough ice between the buoy and the open ocean was unbroken. This is due to the limited sensitivity of the buoy's accelerometer: once the wave energy drops below a certain level, the reported spectrum from the buoy is essentially red noise: energy increases linearly (on a log–log scale) with decreasing frequency. A basic quality control procedure was implemented that removed observations having either period above those thresholds and/or a red noise spectrum.

The buoy also measured its GPS position every 20 min, meteorological parameters (air temperature, wind speed and direction) at 1 m ASL, as well as the buoy heading (magnetic) and sea-surface temperature (actually hull temperature) every hour.

2.2. Enhanced WAM

The model used for this study was the global stand-alone Wave Model (WAM) of the European Centre for Medium Range Weather Forecasting (ECMWF), in its latest operational form as implemented operationally on June 19, 2012 (Bidlot, 2012). The model is run in stand-alone mode on an irregular lat-lon grid with an effective resolution of 28 km, with 36 wave directions (10^o interval) and 36 wave frequencies, from 0.035 Hz (28.6 s). The model time step was 600 s for both source and advection terms. Forcing was by the 6-hourly ERA-Interim 10 m neutral winds, boosted by 5% to account for a known bias in storm track regions (Dee et al., 2011). The model was run from 00 h on 25th August to 00 h on 13th October 2000, output every three hours (*versus* six hours as standard) to match the buoy observations. As in ERA-Interim, data assimilation of ERS-2 wave heights was performed. It used ERS-2 data Ocean Product (OPR) data as obtained from the European Space Agency (ESA) corrected for their known small underestimation using a non-parametric bias estimation with respect to a set of reference buoy data (Dee et al., 2011). Table 1 demonstrates that using corrected ERA-Interim wind globally improved the model hindcast with respect to uncorrected ERA-Interim winds.

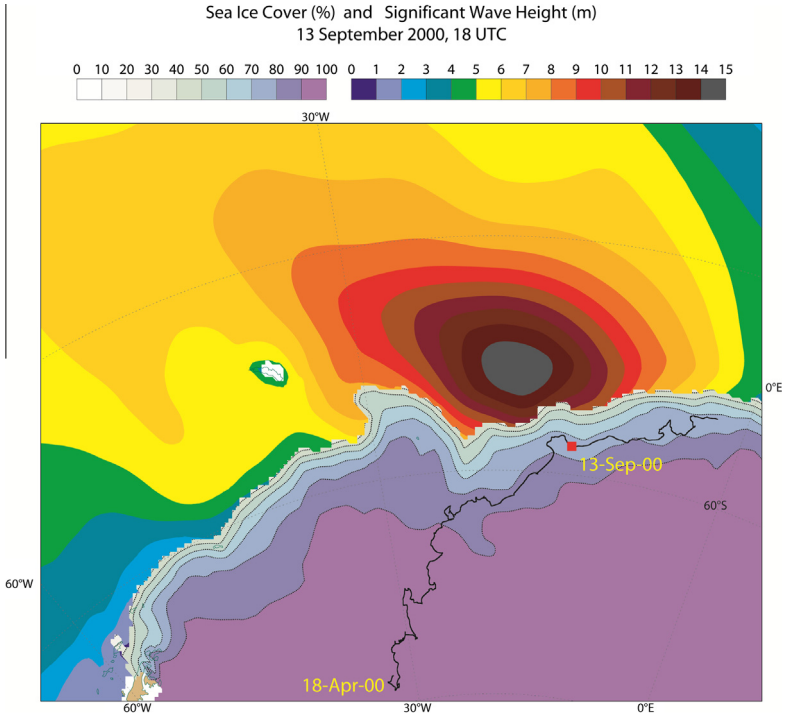

Fig. 1. Buoy track from deployment until transmissions ceased, superimposed on (in ice) the SSM/I ice concentrations (colour bar is% concentration) for that day; and (in open water) the significant wave height from the WAM model at the time of the breakup experienced by the buoy, showing the extreme wave heights intersecting the ice edge at the buoy's longitude.

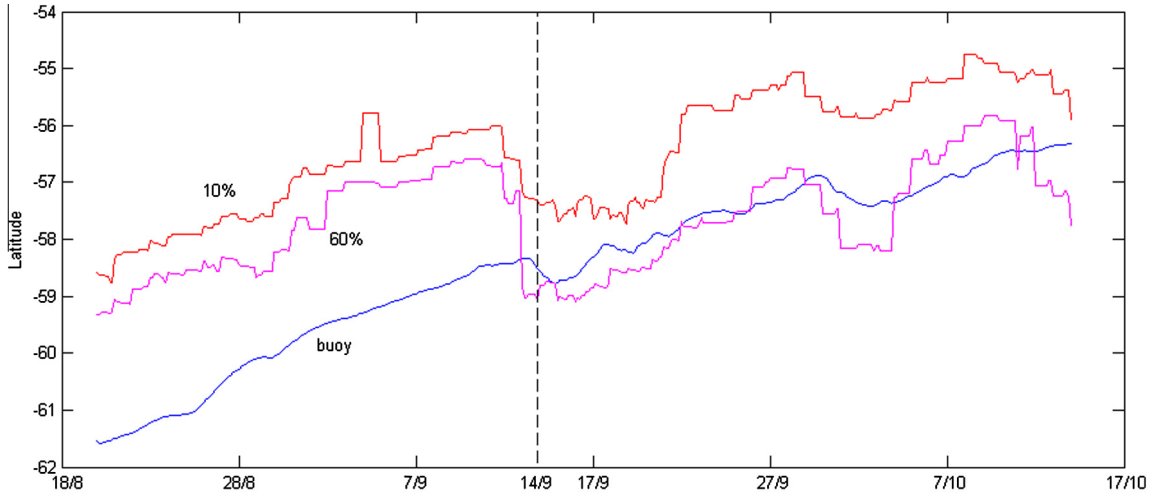

Fig. 2. Time series of the buoy's latitude together with the latitude of the 10% and 60% ice concentration contour at the buoy's longitude (i.e. directly north or south of the buoy location). The vertical dashed line indicates time the pack broke up around the buoy.

Table 1
Comparison of the model first guess prior to assimilation with ERS-2 altimeter wave heights for all observations from 26-08-2000 to 13-10-2000 in terms of bias (model – altimeter), root mean square error (RMSE), Scatter Index (standard deviation of the difference normalised by the altimeter mean) and Correlation Coefficient. The standard mode configuration was used without any added sea ice attenuation scheme.

Number of collocations = 173,218	ERA-Interim winds	1.05*ERA-Interim winds
BIAS (m)	−0.175	−0.002
RMSE (m)	0.367	0.294
Scatter Index	0.127	0.116
Correlation Coefficient	0.973	0.975

WAM was modified for this study to allow waves to propagate into the ice cover. In its operational form, WAM imposes a sea ice mask at the 30% ice concentration contour, defined by ERA-Interim and derived from the NCEP 2D-VAR product. The enhanced scheme was implemented in two forms; firstly to allow the waves to propagate freely in all areas with ice concentration above 30% without any additional wind input, dissipation or non-linear interaction (*i.e.* all source terms turned off) and secondly to implement a damping scheme to attenuate the waves in the ice with the full model physics still active, albeit limited to the relevant open water fraction of the grid box for wind input and dissipation – as in Masson and LeBlond (1989) and Perrie and Hu (1996). Polnikov and Lavrenov (2007) show that the open water nonlinear interaction

term can be used in both open and ice covered areas. The open water wave propagation speed was used: it was assumed that the relevant waves are long enough and the sea ice not too thick and compact that the waves still propagate as if there was no ice (Fox and Haskell, 2001).

The attenuation scheme chosen was the scattering model of Kohout and Meylan (2008), as implemented by Dumont et al. (2011). This treats ice floes as floating elastic plates with prescribed length and thickness and neglects any other energy loss mechanism (for instance through viscous effects). This model was chosen because it was easily implemented into WAM. This two-dimensional (one horizontal, one vertical) model calculates attenuation by comparing transmitted and reflected energies at each interface, using a Monte Carlo scheme to average out resonances. Kohout and Meylan demonstrate that the attenuation coefficient for wave periods between 6 and 16 s is independent of floe size for floes larger than 20 m in length, and only depends on ice thickness and wave period. Namely, if $F(x,f,\theta,t)$ denotes the two-dimensional wave energy spectrum, where x is the two spatial coordinate, f the wave frequency, θ the wave propagation direction and t time, then the wave energy decays exponentially with travel distance in sea ice covered water:

$$F(\boldsymbol{x},f,\theta,t+\Delta t) = F(\boldsymbol{x},f,\theta,t)\exp(-\alpha c_g \Delta t) \tag{1}$$

where c_g is group speed, Δt the model time step, α the dimensional attenuation coefficient:

$$\alpha = ci\frac{a}{\overline{D}} \tag{2}$$

with ci the sea ice concentration, a the non-dimensional attenuation coefficient (a function of wave period and sea ice thickness, h) and $\overline{D}$, the mean size of the floes. The values for the non-dimensional attenuation coefficient a are given by Fig. 6 of Kohout and Meylan (2008), reproduced here as Fig. 3.

To determine $\overline{D}$, knowledge of the floe size distribution is required. We have followed the approach of Dumont et al. (2011), which is based on the renormalisation group method for the fragmentation process of floes in the MIZ. It assumes that mean floe size can be determined when the minimum and the maximum size are known. Following Dumont et al., minimum floe size is set to 20 m (the lower limit for scattering process in the current model) and the maximum to 200 m. The fragmentation process is also controlled by the ability of the floes to break, known as the fragility. This fragility parameter can vary depending on different factors

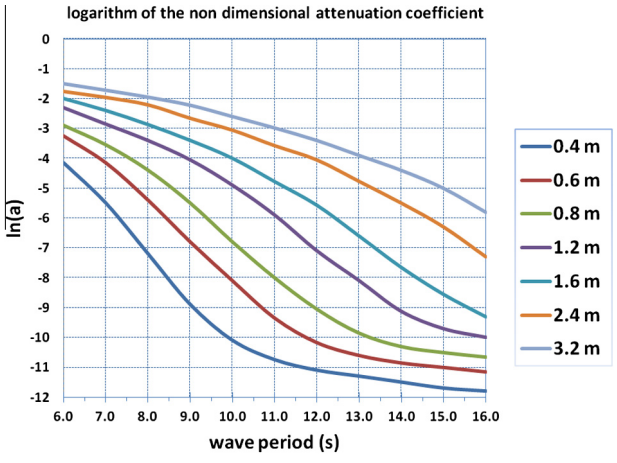

Fig. 3. Natural logarithm of the non-dimensional attenuation coefficient, a, from Kohout and Meylan (2008). It is a function only of wave period (horizontal axis) and sea ice thickness (plotted from 0.4 to 3.2 m) .

that could potentially be modelled but, given the limited sea ice information in the current context, this was set to 0.9. With all these assumptions (as in Dumont et al., 2011), $\overline{D}$ = 36 m.

For this study, the attenuation given in Eq. (1) is applied after the spectrum has been updated by all other source terms. The values of non-dimensional attenuation coefficient a are read from a lookup table, with simple bi-linear interpolation to the exact frequency and ice thickness required. Wave periods outside the prescribed 6–16 s range use a fixed to the respective limit. Though non-physical, this is of little consequence, since (a) waves shorter than 6 s are attenuated to zero almost immediately on encountering sea ice; (b) waves longer than 16 s experience very low attenuation in typical Antarctic ice thicknesses and the curve has become almost flat beyond 12 s (see the red curve in Fig. 3). Finally, since scattering only occurs in a broken ice cover, the model only applies this scheme for ice concentrations below 80%, setting wave energy to zero at higher concentrations.

To connect the ice thickness required for the scattering model to the available data (ci), we impose a concentration-dependent scheme, inspired by Krinner et al. (2010) for the Arctic, which gives an (assumed realistic) decrease of ice thickness towards the ice edge:

$$h = (a_1 + a_2 c_{\min})(a_3 + a_4(ci - c_{\min})) \tag{3}$$

where $c_{\min}$ is the local minimum ice concentration (determined from ERA-Interim ice concentration 1979–2011) and a_{1-4} are chosen (0.2, 2.8, 1.0 and 2.0 respectively). In our implementation, we set $c_{\min}$ = 0 and the relation simplifies to:

$$h = 0.2 + 0.4ci \tag{4}$$

These coefficients give 0.60 m ice thickness at 100% concentration and 0.32 m thickness at the 30% concentration contour. These figures appear reasonable compared to available measurements for the region (Lange et al., 1989; Wadhams et al., 1987; Doble et al., 2003), which suggest a relatively constant level ice thickness of 0.6 m. We examined the sensitivity of modelled wave properties at the buoy by changing the ice thickness to fixed values. The best fit to the buoy data is obtained at ice thicknesses between 0.5 and 0.7 m, again in accordance with the accepted figure.

As a final enhancement to the model, we included attenuation due to the bottom roughness of the ice floes, as parameterised in Kohout et al. (2011) to account for wave energy loss in a compact MIZ. For the portion of the grid box covered by sea ice only, a similar exponential decay as in (1) prevails but with

$$\alpha = C_d H k^2 \tag{5}$$

where H is the wave height of a given wave component, k its corresponding wave number (assumed to be its open water value) and C_d the ice-water drag coefficient. C_d accounts for energy loss due to viscous drag, form drag and energy lost to internal waves under the ice. Kohout et al. quote values for C_d ranging from 1×10^{-3} to 35×10^{-3}. After some testing, we chose C_d as 1×10^{-2}. This term, which we henceforth refer to as 'drag attenuation', was added to that from the scattering model.

3. Results

3.1. Comparison with buoy observations

Fig. 4(a)–(c) compares the buoy observations to the WAM results, in terms of significant wave height (top panel), peak period (middle panel) and mean period (bottom panel). WAM results at the buoy location are plotted for the un-damped free propagation case, for the scattering-only scheme and for both attenuation schemes (scattering + drag) combined.

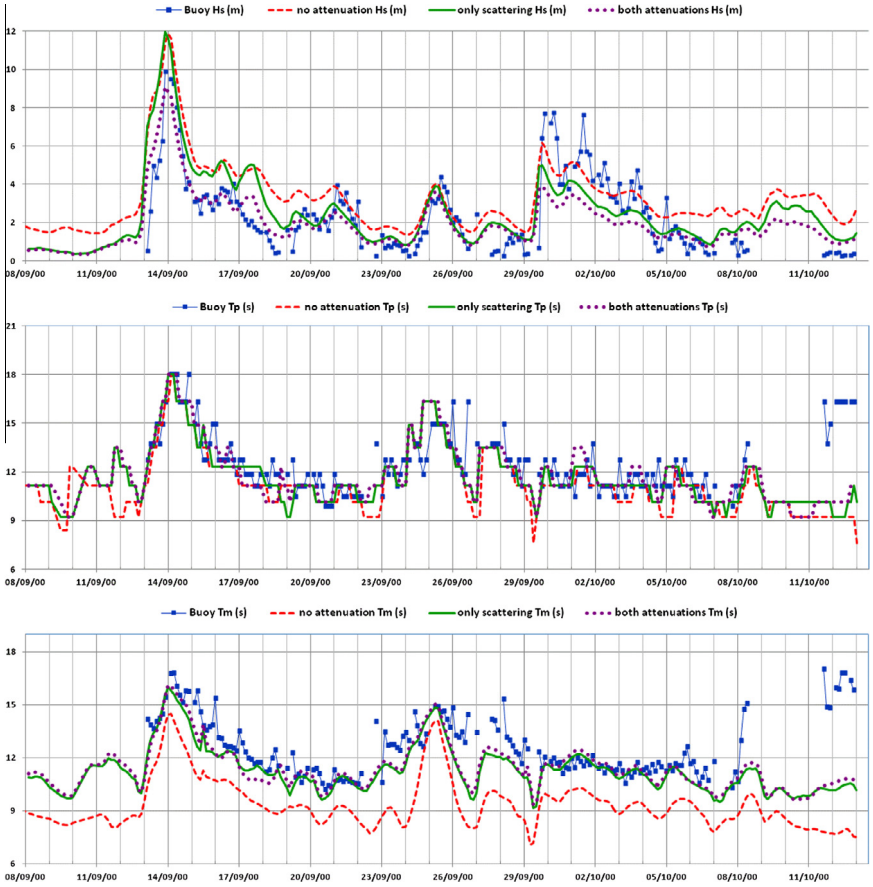

Fig. 4. Significant wave height (top panel), peak period (middle panel) and mean period (bottom panel) over the period of breakup. Results are shown for the buoy observations (blue squares), and the WAM results at the buoy location, for the un-attenuated WAM model (red dashed line), the scattering-only attenuation scheme (green solid line) the combine scattering + drag scheme (magenta dotted line). (For interpretation of the references to color in this figure legend, the reader is referred to the web version of this article.)

Prior to the breakup, the WAM model allows energy to propagate through the ice, whereas the buoy indicates that the pack is still essentially unbroken, blocking the passage of any significant wave energy. During and after the breakup, there is a reasonable correspondence between observations and the damped model results. The model tracks the breakup event closely, though it does not reproduce the very low wave heights (<1 m) observed by the buoy during subsequent calm periods.

Around the beginning of October, observed wave height shows significant variability which is not followed by the model, though the observational data appear to be of good quality. It is possible that small-scale variability in the forcing wind was not well captured by the relatively coarse ERA-Interim forcing (80 km horizontal resolution). In the final week of data transmission, the buoy passed south of the 60% ice concentration contour and observed wave height dropped to almost zero once more. This was not followed by the model, which continued to allow waves to propagate to the buoy's location in accordance with the ice concentration remaining below 80%.

Mean period is well-tracked by both the attenuated models. The un-damped model always exhibits too much high-frequency energy, though the form of the curve is well followed. Peak wave periods are well tracked by both damped and undamped models. Adding the drag attenuation reduces the corresponding wave heights slightly but improves the fit to observed wave periods.

Wave spectra for selected times are shown in Fig. 5(a)–(f), again as measured at the buoy as well as for un-damped and both attenuation schemes. The un-damped model invariably has too much energy at high frequencies (at any frequency above the peak, in fact). The damped models follow the spectral shape of the buoy measurements very well in most cases, though the absolute amplitude is often a factor several times different from reality. The model under-estimates the power of the most energetic events measured by the buoy, probably due to the too-weak ERA-Interim winds, as previously mentioned.

Fig. 5(a) shows the situation just prior to the breakup (12th September). As seen in the timeseries, the model already has wave energy at this location, both un-damped and damped, while the buoy has yet to experience any significant waves. Note the high-frequency peak at $f = 0.36$ Hz, suggesting local wave generation in open water or bobbing/rocking of the floe. Following Czipott and Podney (1989), this frequency represents bobbing of a 0.2 m thick floe or rocking of a 1.0 m thick floe, which is plausible. Fig. 5(b) shows the situation at the time of the breakup (14th September). Both attenuated models represent the spectral peak very well. Adding the ice bottom drag attenuation improves the fit to the tail of the spectrum but slightly under-represents the peak power. Fig. 5() is two days after the break up (17th September). Some locally generated high frequency waves are visible in the attenuated model simulations, since wave generation and dissipation are still active on the open water portion of the grid box. Again the peak of the spectrum is well captured. Fig. 5(d) (22nd September) shows little change in the modelled spectra, while the buoy energy has dropped back to the red noise spectrum (note that because of a limitation in the format of the output model spectra, small model spectral density are truncated to zero, hence the apparent cut-off

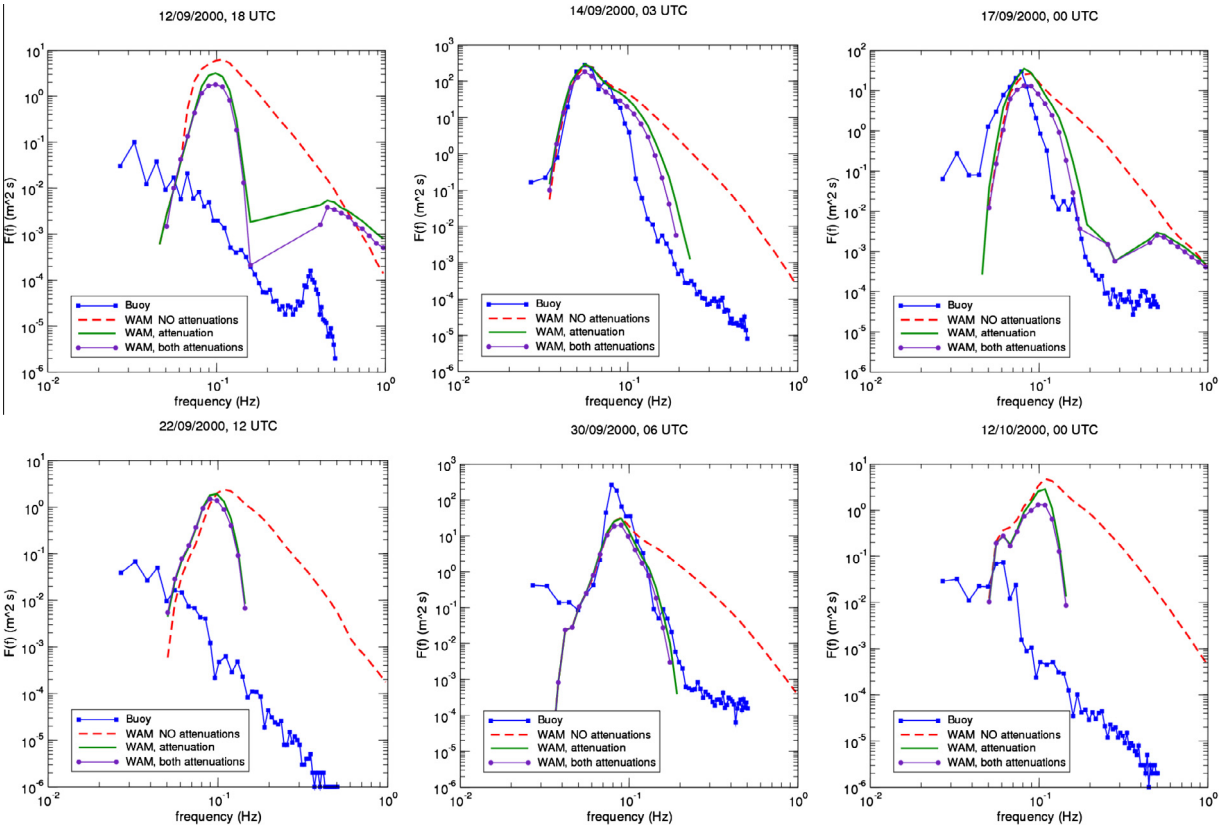

Fig. 5. (a)–(f): Frequency spectrum plots of buoy data and WAM results for selected times. As for Fig. 5, results are shown for the buoy (blue squares), the un-attenuated WAM model (red dashed line), the scattering only scheme (green solid line) the scattering + drag scheme (magenta dotted line). The format used to write out the model spectra ignores small numbers, hence the apparent cut off in the model spectra. (For interpretation of the references to color in this figure legend, the reader is referred to the web version of this article.)

in log–log plot). Fig. 5(e) shows a case where the buoy wave height was well above any modelled value (30th September). Though the observed peak power is not achieved by the model, the attenuated simulations show a good agreement for the high frequency tail. Finally, Fig. 5(f) is very near the end of the buoy's life (12th October), when the buoy observations are once again significantly below the modelled results, close to the accelerometer's noise limit.

3.2. Effects of the damping scheme on waves outside the ice edge

The fit to the altimeter wave height data in the Southern Ocean (south of 50°S) is shown in Table 2. Without sea ice attenuation the model exhibits a tendency to over-estimate wave heights. With the attenuation included, the bias is largely removed and the overall fit to the data improved. Also shown is the case where all waves are blocked if the sea ice concentration is above 30% (as in the current operational WAM). Overall, using the attenuation models gives similar statistical fit to the altimeter data around Antarctica.

The characteristics of the wave field in open water near the ice edge are quite different depending on which model is used, however. Comparing results between runs using both schemes with the un-damped case demonstrates that the presence of the sea ice alters the wave characteristics significantly, with an impact that extends far from the ice itself. The effect of adding the attenuation by ice bottom drag in addition to the scattering scheme is more confined to the ice edge.

In the current operational set-up, the impact of the sea ice is modelled by preventing all waves in areas with sea ice concentration above 30%. The mean difference between the enhanced attenuation model (using both attenuation mechanisms) and this operational configuration is presented in Fig. 6. While the differences are less drastic than the comparison to the un-damped scheme, the influence of the sea ice is particularly visible where lower wave heights and longer periods interact with the ice cover. Moreover, the influence extends far down-wave of areas where the sea ice cover extends northwards. The actual operational wave model at ECMWF is actively coupled to the atmospheric model with a feedback of the waves on the wind. This feedback is linked to the actual shape of the wave model spectra which controls the momentum exchange between the atmosphere and the ocean.

Table 2
Comparison of the model first guess prior to assimilation with ERS-2 altimeter wave heights for all observations south of 50°S from 26-08-2000 to 13-10-2000 in terms of bias (model – altimeter), root mean square error (RMSE), Scatter Index (standard deviation of the difference normalised by the altimeter mean) and Correlation Coefficient. Different model configurations were used.

Number of collocations = 19,860	No attenuation	Attenuation by scattering	Both attenuations	Full blocking for sea ice cover > 30%
BIAS (m)	0.146	0.031	0.007	0.015
RMSE (m)	0.429	0.378	0.376	0.373
Scatter Index	0.106	0.098	0.097	0.097
Correlation Coefficient	0.956	0.963	0.962	0.963

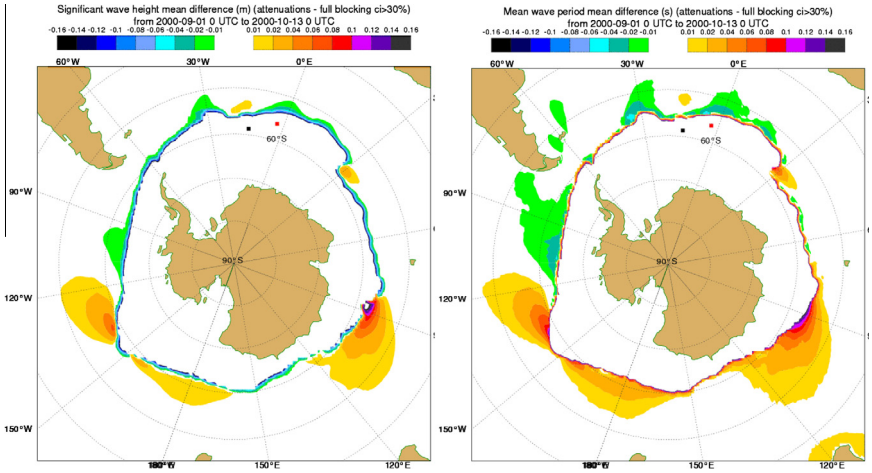

Fig. 6. The effect of implementing the full attenuation (scattering + drag) scheme of the current study *versus* the present operational WAM (wave energy set to zero at *ci* > 30%). The effect is shown for both the mean SWH (left panel) and mean wave period (right panel) from September 1st to October 13th, 2000. The black square indicates the position of the buoy on the September 13th and the red one on October 13th.

Introducing this attenuation model could therefore have an impact on the winds around the sea ice, further enhancing the effect of sea ice on the waves.

The applicability of the attenuation schemes was limited by setting wave energy to zero at sea ice concentrations above 80%. Using any value between 75% and 90% produces essentially identical results at the buoy location. A threshold of 80% concentration gave the best fit to altimeter data, however. Physically, attempting to push the attenuation scheme into regions where scattering is not the dominant energy loss mechanism results in an under-damped model for these areas and that effect is reflected in the open ocean wave field.

4. Discussion and conclusions

We have presented unique field measurements of wave properties prior to, during and after breakup at the Antarctic MIZ. We demonstrate that the enhanced WAM scheme provides a reasonable match to the wave heights, periods and spectra measured at the buoy, using only a simple look-up table for attenuation coefficient supplemented with a parameterisation of the sea ice bottom drag. We acknowledge the simplistic nature of our parameterisation, but this is deliberate since current operational models only have access to very basic sea ice information, such as the NCEP ice concentration data used here.

The model has no concept of floe breaking and thus transmits wave energy to the buoy long before breakup actually occurs there. Since the scattering model is only applicable where the ice is broken, coupling to a simple floe breaking model (such as that implemented by Dumont et al., 2011) would be advantageous. Healing processes in the ice cover, not included in the WAM scheme, will also play a role. This is particularly relevant during periods where the observed wave energy drops to almost nothing while WAM continues to propagate significant wave energy to the buoy (as seen in Figs. 4 and 5). Air temperatures measured by the buoy (and well-followed in the ECMWF reanalysis) indicate episodes of rather low air temperature (between −10 °C and −15 °C) at these times, which suggests that the ice cover will re-freeze in the absence of significant waves to keep the floes broken.

In the meantime, we limit the applicability of the wave propagation to the 0.3–0.8 ice concentration range, as discussed. We note that other forms of ice edge can be modelled with appropriate attenuation schemes (*e.g.* a viscous parameterisation for the vast frazil and pancake zones of the advancing Antarctic sea ice cover, as demonstrated by de Carolis and Desidiero, 2002), with an appropriate switch in the model for the advance/retreat season.

A striking aspect of the buoy measurements is their extreme variability from one measurement interval to the next. Purely instrumental effects are likely not responsible, given the significant averaging performed over the 25 min time-series and the resulting high degrees-of-freedom of the individual spectral measurements. Similarly we would not expect the wave → buoy transfer function to change so radically, then revert to its previous characteristic, between successive measurements. We must thus attribute the variability to real physical changes arising from the complex matrix of materials in a wave-influenced ice edge. The ice cover around the time of breakup is extremely dynamic and the wave field measured by the buoy will depend on the configuration of the surrounding floes, open water regions and the exact form of the ice edge, all too small-scale to be tracked by the model. We might also imagine the buoy passing into the wave shadow of an iceberg (which are numerous in the region) or, conversely, being downwave of an open-water region sufficiently large to raise local waves, seen several times in the data, with significant high frequency (>0.1 Hz) components.

This raises a question of how representative multi-wave buoy measurements – performed to quantify the attenuation coefficient of any given ice cover – can actually be without a detailed knowledge of the ice thickness and concentration to drive an attenuation model. Though such attenuation coefficients (expressed as m^{-1}) can be calculated using a path length defined either by the buoy-to-buoy distance or a virtual along-wave-direction path, the scattering process and the apparently isotropic nature of the resulting wave field (Wadhams et al., 1986) means that the reduction of energy between measurements does not occur due to the attenuation of any given wave packet travelling between the buoys. Rather there is a reduction in wave energy with penetration inward from the ice edge from an incalculable number of contributing scattering paths, with a buoy sampling the energy density at one location. Any real ice edge geometry makes defining this penetration '*x*' difficult, however, and leads us to expect high variability in the measured attenuation coefficient along the ice edge direction for any given penetration. The variability observed here shows that no single 'snapshot' of a real MIZ can be relied on to give definitive results, but that an extended time series with many measurements is required.

The conceptually simple model presented here simulates the observed parameters well, however, smoothing the fluctuations

in observed quantities and allowing the basic process of energy loss to be followed. We expect this enhanced WAM model to be equally applicable in the Arctic Ocean, with appropriate adjustment to the ice thickness scheme (either concentration based, as here, or imposed). Once a floe-breaking and healing scheme is included, the aim is to run the model operationally – following extensive validation - to define the location and width of the wave-influenced zone, and the major wave parameters therein. This will provide valuable guidance for a wide range of scientific studies, monitoring agencies and resource extraction operations.

Acknowledgements

We thank Alison Kohout (NIWA) for discussions regarding the attenuation coefficients in her model, and the Alfred Wegener Institut für Polar- und Meeresforschung, Bremerhaven, for the opportunity to work from F/S "*Polarstern*" during the field experiment and thank the captain and crew for their kind cooperation. The field experiment was supported by the UK Natural Environment Research Council, under grant "Short Timescale Motion of Pancake Ice", number GR3/12952. MJD was funded during the analysis and preparation of this paper by the Office of Naval Research "*Emerging Dynamics of the Marginal Ice Zone*" Departmental Research Initiative, and the "*Arctic Climate Change, Economy and Society*" (ACCESS) project, Grant number 265863 of the "Oceans 2010" call of the European Union Seventh Framework Programme.

References

Ardhuin, F., Tournadre, J., Queffeulou, P., Girard-Ardhuin, F., Collard, F., 2011. Observation and parameterization of small icebergs: drifting breakwaters in the southern ocean. Ocean Modell. 39, 405–410.

Asplin, M.G., Galley, R., Barber, D.G., Prinsenberg, S., 2012. Fracture of summer perennial sea ice by ocean swell as a result of Arctic storms. J. Geophys. Res. 117, C06025. http://dx.doi.org/10.1029/2011JC007221.

Barber, D.G., Galley, R., Asplin, M.G., de Abreu, R., Warner, K.-A., Pućko, M., Gupta, M., Prinsenberg, S., Julien, S., 2009. Perennial pack ice in the southern Beaufort sea was not as it appeared in the summer of 2009. Geophys. Res. Lett. 36, L24501. http://dx.doi.org/10.1029/2009GL041434.

Bennetts, L.G., Squire, V.A., 2012a. On the calculation of an attenuation coefficient for transects of ice-covered ocean. R. Soc. Lond. Proc. Ser. A 468, 136–162. http://dx.doi.org/10.1098/rspa.2011.0155.

Bennetts, L.G., Squire, V.A., 2012b. Model sensitivity analysis of scattering-induced attenuation of ice-coupled wave. Ocean Modell. 45–46, 1–13.

Bidlot, J.-R., 2012. Present status of wave forecasting at ECMWF. in: Proceeding from the ECMWF Workshop on Ocean Waves, 25–27 June 2012.

Broström, G., Christensen, K.H., 2008. Waves and sea ice. Report 5/2008, Norwegian Meteorological Institute, http://met.no/Publikasjoner+2008.b7C_wlfY47.ips.

Czipott, P.V., Podney, W.N., 1989. Measurements of fluctuations in tilt of Arctic ice at the CEAREX oceanography camp: experiment review, data catalog and preliminary results. Final Tech. Report N00014–89-C-0087, US Navy, Washington, DC.

De Carolis, G., Desidiero, D., 2002. Dispersion and attenuation of gravity waves in ice: a two-layer viscous model with experimental data validation. Phys. Lett. A 305, 399–412.

Dee, D.P. et al., 2011. The ERA-Interim reanalysis: configuration and performance of the data assimilation system. Q. J. R. Meteorol. Soc. 137, 553–597. http://dx.doi.org/10.1002/qj.828.

Doble, M.J., 2009. Simulating pancake and frazil ice growth in the Weddell Sea: a process model from freezing to consolidation. J. Geophys. Res. 114, C09003. http://dx.doi.org/10.1029/2008JC004935.

Doble, M.J., Wadhams, P., 2006. Dynamical contrasts between pancake and pack ice, investigated with a drifting buoy array. J. Geophys. Res. 111, C11S24. http://dx.doi.org/10.1029/2005JC003320.

Doble, M.J., Coon, M.D., Wadhams, P., 2003. Pancake ice formation in the Weddell Sea. J. Geophys. Res. 108 (C7), 3209. http://dx.doi.org/10.1029/2002JC001373.

Dumont, D., Kohout, A., Bertino, L., 2011. A wave-based model for the marginal ice zone including a floe breaking parameterization. J. Geophys. Res. 116, C04001. http://dx.doi.org/10.1029/2010JC006682.

Fox, C., Haskell, T.G., 2001. Ocean wave speed in the Antarctic MIZ. Ann. Glaciol. 33.

Francis, O.P., Panteleev, G.G., Atkinson, D.E., 2011. Ocean wave conditions in the Chukchi sea from satellite and in situ observations. Geophs. Res. Lett. 38, L24610. http://dx.doi.org/10.1029/2011GL049839.

Kohout, A.L., Meylan, M.H., 2008. An elastic plate model for wave attenuation and ice floe breaking in the marginal ice zone. J. Geophys. Res. 113, C09016. http://dx.doi.org/10.1029/2007JC004434.

Kohout, A.L., Meylan, M.H., Plew, D.R., 2011. Wave attenuation in a marginal ice zone due to the bottom roughness of ice floes. Ann. Glaciol. 52 (57), 118–122.

Krinner, G., Rinke, A., Dethloff, K., Gorodetskaya, I.V., 2010. Impact of prescribed Arctic sea ice thickness in simulations of the present and future climate. Clim. Dyn. 35, 619–633.

Lange, M.A., Ackley, S.F., Wadhams, P., 1989. Development of sea ice in the Weddell Sea. Ann. Glaciol. 12, 92–96.

Liu, A.K., Holt, B., Vachon, P.W., 1991. Wave propagation in the marginal ice zone: Model predictions and comparisons with buoy and synthetic aperture radar data. J. Geophys. Res. 96 (C3), 4605–4621.

Masson, D., LeBlond, P.H., 1989. Spectral evolution of wind-generated surface gravity waves in a dispersed ice field. J. Fluid Mech. 202, 111–136.

Perovich, D.K., Richter-Menge, J.A., Jones, K.F., Light, B., 2008. Sunlight, water, and ice: extreme Arctic sea ice melt during the summer of 2007. Geophys. Res. Lett. 35, L11501. http://dx.doi.org/10.1029/2008GL034007.

Perrie, W., Hu, Y., 1996. Air-ice-ocean momentum exchange. Part 1: Energy transfer between waves and ice floes. J. Phys. Oceanogr. 26, 1705–1720.

Polnikov, V.G., Lavrenov, I.V., 2007. Calculation of the nonlinear energy transfer through the wave spectrum at the sea surface covered with broken ice. Oceanology 47, 334–343.

Squire, V.A., 2007. Of ocean waves and sea–ice revisited. Cold Reg. Sci. Technol. 49, 110–133.

Squire, V., Moore, S.C., 1980. Direct measurement of the attenuation of ocean waves by pack ice. Nature 283 (5745), 365–368.

Squire, V.A., Dugan, J.P., Wadhams, P., Rottier, P.J., Liu, A.K., 1995. Of ocean waves and sea ice. Annu. Rev. Fluid Mech. 27, 115–168.

Steele, M., 1992. Sea ice melting and floe geometry in a simple ice–ocean model. J. Geophys. Res. 97 (C11), 17,729–17,738.

Steer, A., Worby, A.P., Heil, P., 2008. Observed changes in sea–ice floe size distribution during early summer in the western Weddell Sea. Deep-Sea Res. Part II 55, 933–942.

Toyota, T., Haas, C., Tamura, T., 2011. Size distribution and shape properties of relatively small sea-ice floes in the Antarctic marginal ice zone in late winter. Deep Sea Res. II. http://dx.doi.org/10.1016/j.dsr2.2010.10.034.

Vaughan, G.L., Squire, V.A., 2011. Wave induced fracture probabilities for Arctic sea ice. Cold Reg. Sci. Technol. 67, 31–36.

Wadhams, P., Squire, V.A., Ewing, J.A., Pascal, R.W., 1986. The effect of the marginal ice zone on the directional wave spectrum of the ocean. J. Phys. Oceanogr. 16, 358–376.

Wadhams, P., Lange, M.A., Ackley, S.F., 1987. The ice thickness distribution across the Atlantic sector of the Antarctic Ocean in mid-winter. J. Geophys. Res. 92 (C13), 14,535–14,552.

Wadhams, P., Squire, V.A., Goodman, D.J., Cowan, A.M., Moore, S.C., 1988. The attenuation rates of ocean waves in the marginal ice zone. J. Geophys. Res. 93 (C6), 6799–6818.

Williams, T., Bennetts, L., Dumont, D., Squire, V., Bertino, L., 2012. Towards the inclusion of wave–ice interactions in large-scale models for the marginal ice zone. ArXiv e-prints, arXiv:1203.2981W.